Dalton Transactions

ROYAL SOCIETY OF CHEMISTRY

PAPER

View Article Online
View Journal | View Issue

Cite this: *Dalton Trans.*, 2026, **55**, 2624

Molten salt synthesis of Eu^{2+}-doped $Sr_5(PO_4)_3Cl$ in air atmosphere: europium self-reduction and optical properties

Simona Bendziute,[a] Jonas Stadulis,[a] Guna Doke,[a,b] Guna Krieke,[a,b] Andris Antuzevics,[b] Vladimir Pankratov,[b] Inga Grigoraviciute,[a] Arturas Katelnikovas[a] and Aleksej Zarkov*[a]

In the present work, a series of Eu^{2+}-doped $Sr_5(PO_4)_3Cl$ powders with varying Eu content was synthesized by the molten salt method in an air atmosphere. The self-reduction of Eu^{3+} to Eu^{2+} occurred during the phase transformation of starting $Sr_3(PO_4)_2$:Eu to $Sr_5(PO_4)_3Cl$:Eu in molten $SrCl_2$. The synthesis conditions were optimized in terms of reaction temperature, time, and precursor-to-flux ratio. The optical properties of the obtained materials were investigated through photoluminescence, thermally stimulated luminescence, and persistent luminescence decay measurements. Regardless of the Eu concentration, the resulting powders possessed a dominating Eu^{2+}-related broadband emission with a maximum at 445 nm; however, significantly weaker emission in the red region was also detected, suggesting incomplete reduction of Eu^{3+} to Eu^{2+}. Minor emission tunability was achieved by varying the excitation wavelength, which allows for the elimination of Eu^{3+} emission. The analysis of trap properties indicated the presence of two types of traps. Although all obtained E_a values were deep, a weak persistent luminescence signal of Eu^{2+} can be detected for several hours after X-ray irradiation.

Received 3rd November 2025,
Accepted 19th January 2026

DOI: 10.1039/d5dt02634b

rsc.li/dalton

1. Introduction

The Eu^{2+} ion is one of the most frequently used activators in luminescent materials due to its exceptional optical properties, which include broad excitation and absorption bands, as well as intense broadband emission, originating from the dipole and spin allowed $4f^6 5d^1 \rightarrow 4f^7$ transitions.[1,2] Moreover, the local coordination environment has a significant effect on the emission of Eu^{2+} ions, resulting in the matrix-dependent luminescence covering a broad spectral range from blue to infrared.[3] Due to these properties, Eu^{2+}-doped materials have been widely investigated for applications in white light-emitting diodes, scintillators, long afterglow phosphors, *etc.*[4–6]

Most frequently, Eu^{2+}-activated phosphors are synthesized in a reducing atmosphere, which is caused by the need to convert Eu ions from trivalent to divalent oxidation state. However, some specific matrices allow the reduction of Eu^{3+} to Eu^{2+} in the air atmosphere, which is defined as Eu self-reduction.[7] The self-reduction phenomenon has several requirements for the matrix, which usually include: (I) the absence of oxidizing ions in the host compound; (II) the Eu^{3+} dopant replaces a divalent cation in the host; (III) the substituted cation has a similar radius to that of Eu^{2+}; and (IV) the host material has a crystal structure, based on tetrahedral anion groups ($[SiO_4]^{4-}$, $[PO_4]^{3-}$ or $[AlO_4]^{5-}$, *etc.*).[8] Obviously, the self-reduction strategy offers multiple advantages over the use of reducing environment in terms of lower price, safer and easier handling; however, the choice of suitable hosts is limited. Although the self-reduction of Eu^{3+} is most frequently incomplete, resulting in mixed-valence materials, in some cases, this fact can be considered as an advantage, *e.g.*, realizing a dual-emitting material with tunable luminescence.[9] Tuning the emission by varying excitation wavelength, temperature, or pressure can result in selective or simultaneous emission of Eu^{2+}/Eu^{3+} species. Such materials can be used for anti-counterfeiting or luminescent thermometry and manometry.[10–12]

$Sr_5(PO_4)_3Cl$ is a perfect candidate for realizing Eu^{3+} to Eu^{2+} self-reduction since this host meets all the above-mentioned matrix requirements. Moreover, the ionic radii of Sr^{2+} and Eu^{2+} (1.26 Å and 1.25 Å for VIII-fold coordination, as expected in $Sr_5(PO_4)_3Cl$, respectively) are almost identical.[13] $Sr_5(PO_4)_3Cl$ belongs to the family of apatite-structure materials, known for their structural flexibility and ability to adopt both isovalent and aliovalent ions.[14,15] For this reason, many alkaline earth apatite-type phosphors were previously developed by doping the matrix with various rare-earth ions.[9,16–19] The synthesis of

[a]*Institute of Chemistry, Vilnius University, Naugarduko 24, LT-03225 Vilnius, Lithuania. E-mail: aleksej.zarkov@chf.vu.lt*
[b]*Institute of Solid State Physics, University of Latvia, Kengaraga 8, LV-1063 Riga, Latvia*

Eu^{2+}-doped $Sr_5(PO_4)_3Cl$ is also described in the literature; however, the reported synthesis conditions and resulting luminescent properties vary significantly. Although most studies combine the conventional solid-state reaction method with a reducing H_2 or CO atmosphere,[20–25] there are few reports on the synthesis of mixed-valence Eu-doped $Sr_5(PO_4)_3Cl$ in air.[26–28] For instance, Deng *et al.* reported Eu^{2+} emission in $Sr_5(PO_4)_3F_xCl_{1-x}$ solid solutions synthesized in air; however, the spectral range corresponding to Eu^{3+} emission was not shown.[27] Mixed-valence $Sr_5(PO_4)_3Cl$:Eu was previously synthesized by Chen *et al.* by the solid-state reaction method in air.[28] The observed Eu^{2+}/Eu^{3+} emission was concentration-dependent, allowing for the achievement of tunable luminescence by varying Eu content. A wet-chemical approach to the synthesis of Eu^{2+}-doped $Sr_5(PO_4)_3Cl$ was demonstrated in a very few works. Song *et al.* used hydrazine as a reducing agent under hydrothermal conditions.[29] The ratio of Eu^{2+} and Eu^{3+} emission was dependent on the hydrazine concentration, chemical reaction duration, and excitation wavelength. Zou *et al.* employed a solvothermal approach using various organic additives, which makes the reason for Eu^{3+} reduction unclear.[30]

In the present work, we report the synthesis of Eu^{2+}-doped $Sr_5(PO_4)_3Cl$ by the molten salt method in an air atmosphere. The self-reduction of Eu^{3+} to Eu^{2+} occurred during the phase transformation of $Sr_3(PO_4)_2$:Eu precursor to $Sr_5(PO_4)_3Cl$:Eu in molten $SrCl_2$. The luminescent properties of the resulting materials were studied in terms of steady-state and kinetic luminescence, thermally stimulated luminescence, and persistent luminescence decay measurements.

2. Experimental

2.1. Synthesis

The synthesis of $Sr_5(PO_4)_3Cl$:Eu powders was performed by a two-step procedure. In the first step, a series of $Sr_3(PO_4)_2$ powders with different amounts of Eu^{3+} was synthesized by the co-precipitation method, followed by high-temperature annealing. The Eu doping level (0.1, 0.25, 0.5, 1.0, and 2.0 mol%) was calculated with respect to Sr^{2+} ions. $Sr(NO_3)_2$ (≥99%, Roth), $(NH_4)_2HPO_4$ (≥98%, Roth), and $Eu(NO_3)_3{\cdot}6H_2O$ (99.9%, Acros Organics) were used as starting materials. For the synthesis, the appropriate amounts of $Sr(NO_3)_2$ and $Eu(NO_3)_3{\cdot}6H_2O$ were dissolved in 50 mL of deionized water to obtain a solution with a total concentration of metal ions of 0.6 M. In parallel, $(NH_4)_2HPO_4$ was dissolved in 50 mL of deionized water in a separate beaker to obtain a 0.4 M solution. The pH value of the phosphate solution was adjusted to 10 with ammonia solution (NH_4OH, 25%, Roth). The solution of metal nitrates was rapidly added to the $(NH_4)_2HPO_4$ solution, resulting in the formation of white precipitates. The obtained precipitates were aged for 10 min, filtered, washed with deionized water to remove residual counterions, and dried in an oven at 80 °C overnight. The resulting powders were ground in an agate mortar and annealed in a furnace in air at 1100 °C for 5 h at a heating rate of 5 °C min^{-1}.

In the second step, $Sr_3(PO_4)_2$:Eu was converted to $Sr_5(PO_4)_3Cl$:Eu by the molten salt method. For the synthesis, 1 g of $Sr_3(PO_4)_2$:Eu was thoroughly mixed with $SrCl_2$ (≥95%, Thermo Scientific) at a mass ratio of 1 : 2, respectively. The obtained mixture was transferred into the corundum crucible, covered with a lid, heated in air to 1000 °C at a rate of 5 °C min^{-1}, and annealed at this temperature for 1 h. After the annealing procedure, the furnace was cooled down naturally. The melts were washed with hot deionized water to dissolve residual $SrCl_2$. Finally, the products were dried in an oven at 80 °C and ground in a mortar. The $Sr_5(PO_4)_3Cl$:Eu samples in the text are denoted according to the nominal Eu content in $Sr_3(PO_4)_2$:Eu precursors.

2.2. Characterization

Powder X-ray diffraction (XRD) data of the synthesized powders were obtained using a Rigaku MiniFlex II diffractometer (Cu-K_α, λ = 1.5419 Å) working in the Bragg–Brentano ($\theta/2\theta$) geometry. The data were collected within the 10–60° 2θ angle range with a 5° min^{-1} scan speed.

Fourier transform infrared (FTIR) spectra were taken in the 4000–400 cm^{-1} range using a Bruker ALPHA-FTIR spectrometer.

Raman spectra were recorded by a combined Raman and scanning near-field optical microscope WiTec Alpha 300 R equipped with a 532 nm excitation laser source.

The morphology of the synthesized powders and elemental distribution were studied by scanning electron microscopy (SEM) with coupled energy-dispersive X-ray spectroscopy (EDX) using a FlexSEM 1000 II microscope.

The Eu content in the synthesized products was quantified by inductively coupled plasma optical emission spectrometry (ICP-OES) using a PerkinElmer Optima 7000DV spectrometer. The samples prior to analysis were dissolved in 5% nitric acid (HNO_3, Rotipuran® Supra 69%, Roth).

The photoluminescence excitation (PLE) and photoluminescence emission (PL) spectra were measured using the Edinburgh Instruments FLS980 spectrometer equipped with double excitation and emission monochromators, a 450 W Xe arc lamp, a cooled (−20 °C) single-photon counting photomultiplier (Hamamatsu R928P), and mirror optics for the powder samples. The PL spectra were corrected using a correction file obtained from a tungsten incandescent lamp certified by NPL (National Physics Laboratory, UK). The excitation spectra were corrected by a reference detector. PL decay curves were measured using the same Edinburgh Instruments FLS980 spectrometer.

For PL decay measurements, a picosecond pulsed diode laser from Edinburgh Instruments (EPL-405) was used as an excitation source (λ_{ex} = 405 nm).

Quantum yields (QY) were determined using a Teflon-coated integrating sphere and a barium sulfate ($BaSO_4$ for white standard DIN 5033, Merck) as a white standard.[31]

Thermally stimulated luminescence (TSL) glow curves and spectra, along with persistent luminescence decay measurements, were conducted using the Lexsyg research TSL/OSL

reader (Freiberg Instruments GmbH), equipped with a photomultiplier tube R13456 from Hamamatsu and an Andor SR-303i-B spectrometer paired with a DV420A-BU2 CCD camera. For irradiation sources, a VF-50 J/S X-ray tube (40 kV, 0.5 mA, tungsten anode) or a Q-switched short-pulsed UV laser DTL-389QT (263 nm) from the Laser-Compact Group was employed. The system operated with a linear heating rate of 1 °C s^{-1}. Isothermal afterglow decay was measured at 25 °C. To eliminate any effects from previously stored energy, the samples were preheated to 300 °C prior to each measurement.

Room-temperature EPR spectra were measured using a Bruker ELEXSYS-II E500 CW-EPR spectrometer operating at X- (9.834 GHz) and Q- (34.01 GHz) microwave frequency bands and 1 mW microwave power. The magnetic field modulation amplitude was 0.1 mT with a 100 kHz modulation frequency. An X-ray tube operated at 45 kV and 10 mA for 30 min was used to investigate the radiation-induced radicals in the samples. Afterwards, the irradiated samples were isochronally annealed in an air atmosphere, maintaining each temperature step for 10 min, using a custom-built furnace. EPR spectra simulations were performed using EasySpin software.[32]

3. Results and discussion

The XRD pattern of $Sr_3(PO_4)_2$ precursor doped with 1 mol% of Eu is shown in Fig. S1 as a representative. As seen, the diffraction peaks match very well with the standard XRD data of rhombohedral $Sr_3(PO_4)_2$. The PL spectra of Eu-doped $Sr_3(PO_4)_2$ powders are shown in Fig. S2. Evidently, under a 270 nm excitation, the spectra are dominated by sharp emission lines ranging from orange to the NIR region and associated 4f–4f transitions in Eu^{3+} ions, specifically $^5D_0 \rightarrow {}^7F_{0-6}$.[33] Only insignificant emission related to Eu^{2+} was observed, indicating that Eu ions in the precursor are primarily found in a trivalent state, and a low degree of Eu reduction was achieved during the synthesis of $Sr_3(PO_4)_2$. This observation agrees well with a previous study by Szyszka *et al.*, who reported a weak Eu self-reduction in sol–gel derived $Sr_3(PO_4)_2$, resulting in a co-existence of mixed-valence Eu ions.[34]

The synthesis of $Sr_5(PO_4)_3Cl$:Eu^{2+} was optimized, aiming to maximize the level of Eu self-reduction and obtain materials with the lowest Eu^{3+} contribution to the PL spectra. The synthesis conditions were optimized in terms of reaction temperature, time, and precursor-to-flux ratio using a $Sr_3(PO_4)_2$ precursor doped with 0.1 mol% of Eu. The XRD patterns, normalized PL and PLE spectra of $Sr_5(PO_4)_3Cl$:Eu powders synthesized at temperatures from 900 to 1100 °C are shown in Fig. S3. Single-phase materials were obtained in all cases; however, the sample synthesized at 900 °C demonstrated the most intense Eu^{3+} emission, while the difference between the other 2 samples was insignificant. The reaction time in the range from 1 to 10 h did not affect the phase purity (Fig. S4a) and the Eu^{2+}/Eu^{3+} emission ratio; all the PL spectra were virtually the same (Fig. S4b). Finally, the influence of the precursor-to-flux ratio in the range from 1 : 1 to 1 : 10 was investigated. It turned out that the precursor-to-flux ratio did not affect the phase purity of the final products, and the single-phase materials were obtained in all cases (Fig. S5a). On the other hand, the intensity of Eu^{3+} emission increased with an increase in flux content (Fig. S5b). Based on the obtained results, a final series of $Sr_5(PO_4)_3Cl$:Eu samples with varying Eu content was synthesized.

Fig. 1a shows the XRD patterns of $Sr_5(PO_4)_3Cl$:Eu^{2+} powders obtained by the molten salt synthesis. While the main diffraction peaks match very well with the standard XRD data of hexagonal $Sr_5(PO_4)_3Cl$, with a $P6_3/m$ space group (#176), an additional peak was observed at *ca.* 30° for the samples with higher Eu concentrations starting from 0.5 mol%. The intensity of this peak correlated with the amount of Eu in the starting material; an increase in Eu content corresponded to an increase in intensity. This peak cannot be ascribed to potential secondary phases such as $Sr_3(PO_4)_2$, $EuPO_4$, EuOCl, or Eu_4OCl_6. The impurity phase was identified as monoclinic Eu_2O_3 (PDF-5 #00-034-0072), and the peaks at 14.85° and 29.95° correspond to the (−201) and (−402) planes, respectively. The molten salt method is known for its ability to stabilize metastable materials;[35] moreover, it was shown that monoclinic Eu_2O_3 crystals can be grown from NaF flux.[36] We also repeated the synthesis several times; however, the results were reproducible in terms of the presence of the extra peak.

Vibrational spectroscopy was further employed to confirm the crystal structure and verify the purity of the synthesized powders. The FTIR spectra are shown in Fig. 1b in the spectral range from 1400 to 400 cm^{-1}, since there were no absorption bands in the rest of the spectra. The spectra match well with the results presented in the literature;[9,29,37] four groups of bands are clearly seen. The absorption bands in the range from *ca.* 1110 to 958 cm^{-1} belong to the asymmetric P–O stretching mode (ν_3) of the phosphate tetrahedra, while the band centered at 946 cm^{-1} is ascribed to the symmetric P–O stretching mode (ν_1). The two bands in the range from *ca.* 615 to 500 cm^{-1} are attributed to the O–P–O bending mode (ν_4) of PO_4 units, and the band centered at 459 cm^{-1} is ascribed to the ν_2 O–P–O bending mode. FTIR spectroscopy did not demonstrate any significant differences between the samples based on the Eu content; moreover, the presence of any impurity phase was not detected. This suggests that the impurity phase detected by XRD does not belong to phosphate materials. The Raman spectra of the samples are given in Fig. 1c. Four groups of bands can be seen in all spectra, which agrees with the results of FTIR spectroscopy. The signals observed in the ranges of 400–460, 560–620, and 1010–1080 cm^{-1} are ascribed to the ν_2, ν_4, and ν_3 vibrational modes of the phosphate group, respectively.[25] The most intense band centered at 955 cm^{-1} corresponds to the ν_1 vibrational mode.

The representative SEM images of the synthesized samples are shown in Fig. 2a–c. It is seen that the powders consist of polygonal particles with clearly visible facets. The observed morphology is characteristic of apatite-structure materials prepared by the flux method.[38,39] The size of the particles varied

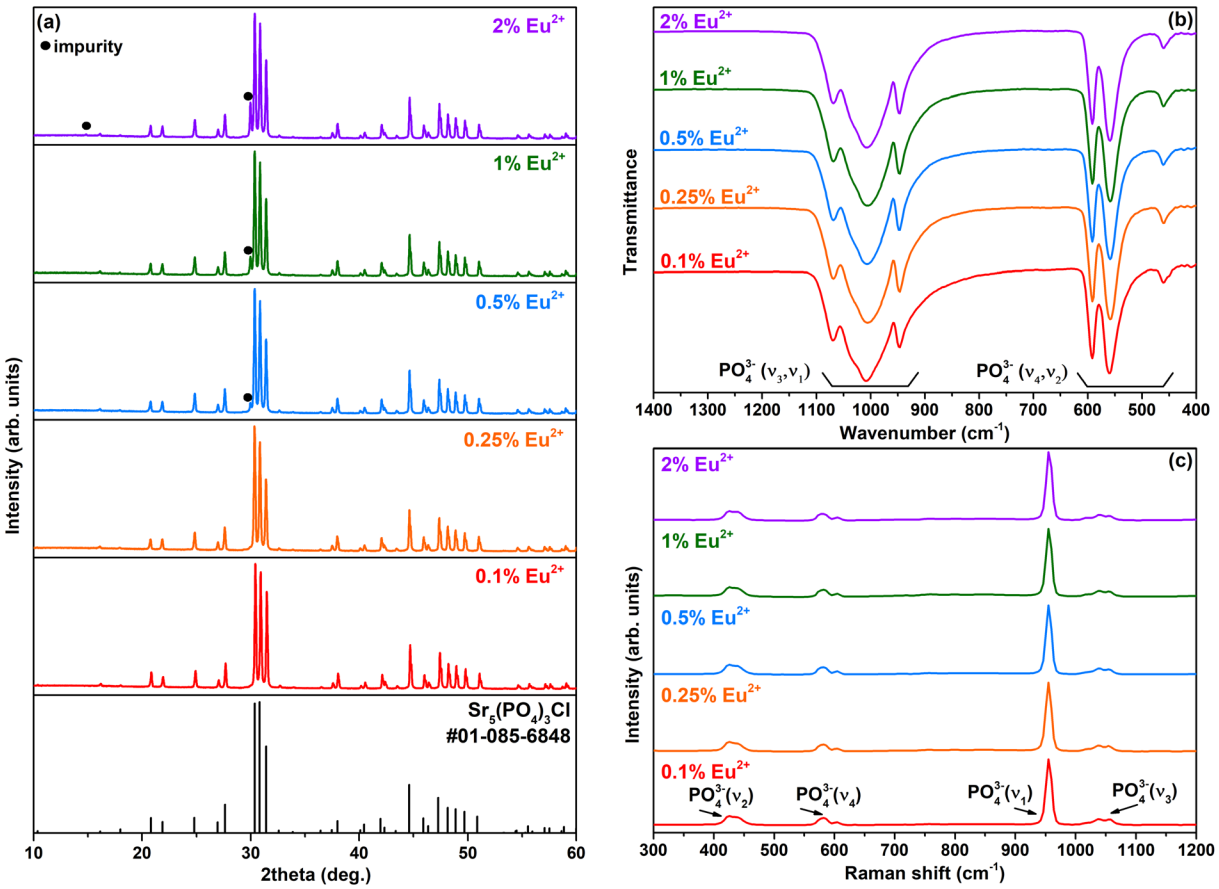

Fig. 1 XRD patterns (a), FTIR spectra (b), and Raman spectra (c) of $Sr_5(PO_4)_3Cl$:Eu powders containing different amounts of Eu.

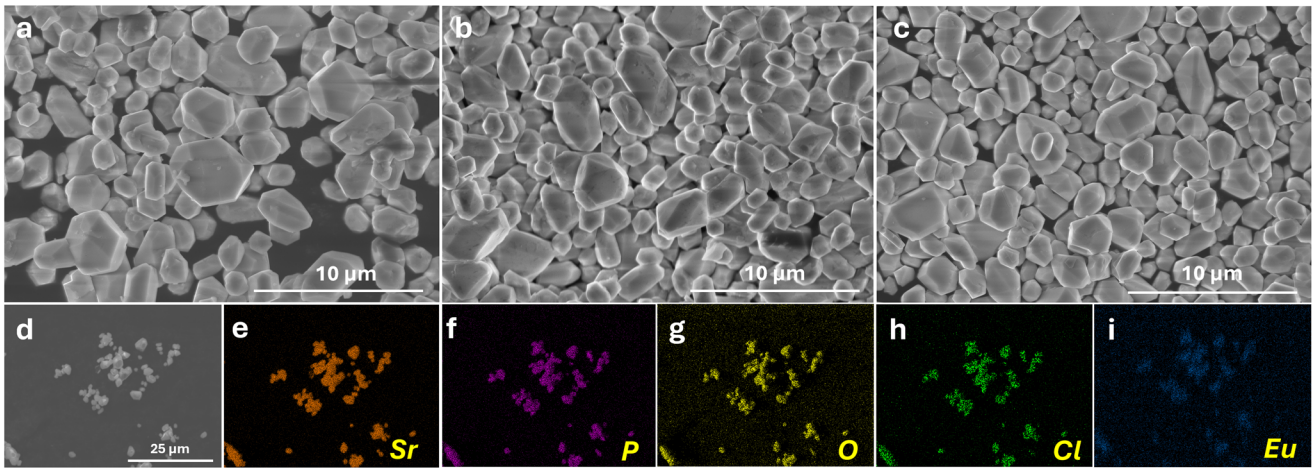

Fig. 2 SEM images of $Sr_5(PO_4)_3Cl$:Eu powders containing 0.1 mol% (a), 0.25 mol% (b), and 2 mol% (c) of Eu; EDX mapping of $Sr_5(PO_4)_3Cl$:0.25%Eu (d–i).

in the range from approximately 1 to 6 μm. The amount of Eu did not influence the shape and the size of the obtained particles. Fig. 2d–i demonstrate the EDX mapping of the $Sr_5(PO_4)_3Cl$:0.25%Eu sample. The results confirmed uniform distribution of all elements; there were no visible regions with high content of particular elements and the absence of others. However, a closer examination of the SEM images of the samples with a higher Eu content revealed the presence of some plate-like particles. EDX mapping confirmed that these particles do not contain Sr, P, and Cl and can be attributed to

Eu_2O_3 (Fig. S6). This type of particle was observed exclusively in samples containing the impurity phase and goes hand in hand with the results of XRD analysis. The oriented shape of Eu_2O_3 particles can explain the relatively high intensity of the impurity peaks in the XRD patterns due to preferred orientation (Fig. 1a).

The phase conversion from starting $Sr_3(PO_4)_2$:Eu to final $Sr_5(PO_4)_3Cl$:Eu occurred in molten $SrCl_2$, which provides a significant excess of the Sr^{2+} ions in the reaction medium. It is reasonable to suggest that Sr^{2+} ions compete with the Eu ions for the site occupancy in the crystal lattice of $Sr_5(PO_4)_3Cl$ during the crystallization process, which could lead to "wash out" and incomplete transfer of Eu from precursor to the product. Elemental analysis of $Sr_5(PO_4)_3Cl$:Eu powders was performed by ICP-OES in order to determine the doping level experimentally. It should be noted that the Sr/P ratio in $Sr_3(PO_4)_2$ and $Sr_5(PO_4)_3Cl$ is 1.5 : 1 and 1.67 : 1, respectively.

Table 1 Results of ICP-OES analysis of $Sr_5(PO_4)_3Cl$:Eu powders

Nominal Eu content in $Sr_3(PO_4)_2$:Eu (mol%)	Nominal Eu content in $Sr_5(PO_4)_3Cl$:Eu (mol%)	Determined Eu content in $Sr_5(PO_4)_3Cl$:Eu (mol%)
0.10	0.090	0.042
0.25	0.22	0.21
0.50	0.45	0.45
1.0	0.90	0.88
2.0	1.8	1.77

Such a difference suggests that a fraction of Sr^{2+} ions required to form $Sr_5(PO_4)_3Cl$ is absorbed from the flux, since the amount of phosphate ions is fixed. The same behavior was previously demonstrated for converting amorphous calcium phosphate with a Ca/P ratio of 1.5 : 1 to $Ca_5(PO_4)_3Cl$ in molten KCl–$CaCl_2$.[38] The difference between the Sr/P ratio in the starting and final materials also reduces the percentage of Eu ions in the final material compared to the precursor, *e.g.*, 1 mol% of Eu in $Sr_3(PO_4)_2$ corresponds to 0.898 mol% in $Sr_5(PO_4)_3Cl$. The ICP-OES analysis results (Table 1) indicate that the actual Eu content in the product is very close to the theoretical values, and the Eu loss in the form of Eu chloride or other water-soluble side-products during the phase conversion is insignificant. It is worth noting that ICP-OES provides the concentration of elements in the bulk material and does not prove the presence of all Eu ions in the $Sr_5(PO_4)_3Cl$ matrix. Moreover, the actual (Sr + Eu)/P ratio in $Sr_5(PO_4)_3Cl$:Eu should be slightly lower than 1.67 : 1 due to the substitution of Sr^{2+} ions by aliovalent Eu^{3+}, forming Sr^{2+} vacancies.

The PLE spectra of $Sr_5(PO_4)_3Cl$:Eu samples for λ_{em} = 455 nm are shown in Fig. 3a. The observed spectra are typical of Eu^{2+} and consist of the broad bands with a maximum at approximately 270 nm. The highest intensity was observed for the sample doped with 0.25% Eu, while the lowest intensity was observed for the sample with the highest Eu content. The spectra of the samples with higher Eu content (1% and 2%) also demonstrate a slight decrease in intensity at 362 and 394 nm, which is associated with the typical excitation bands

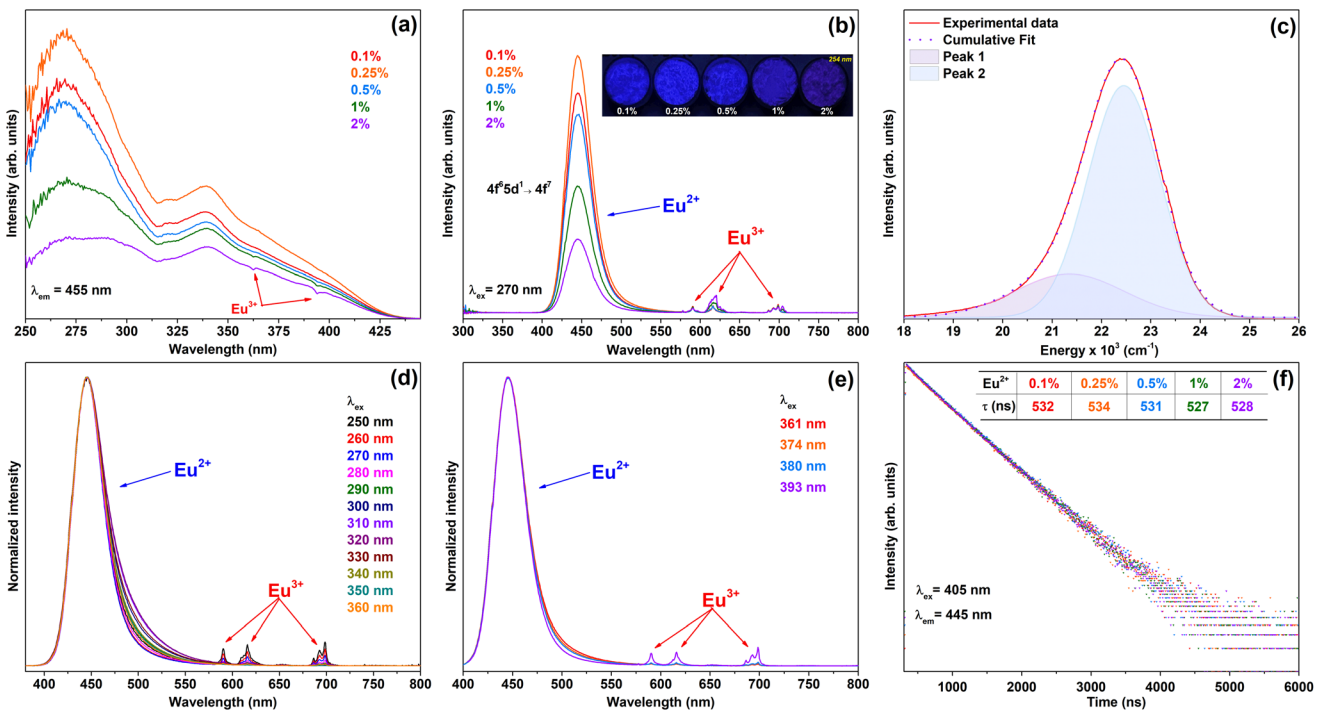

Fig. 3 PLE spectra (a); PL spectra. Inset: images of $Sr_5(PO_4)_3Cl$:Eu under 254 nm irradiation (b); spectral deconvolution of the PL spectrum (c); normalized PL spectra under varying λ_{ex} (d); normalized PL spectra under excitation wavelengths characteristic of Eu^{3+} (e); and decay curves (f) of $Sr_5(PO_4)_3Cl$:Eu powders.

of Eu^{3+}. This indicates the presence of Eu^{3+} ions and the co-existence of both oxidation states. The PL spectra of the samples excited at 270 nm (Fig. 3b) are dominated by a broad band centered at 445 nm, which is attributed to the $[Xe]4f^65d^1 \rightarrow [Xe]4f^7$ transition of Eu^{2+}.[2] The most intense emission was observed for the $Sr_5(PO_4)_3Cl$:0.25%Eu sample, followed by a decrease in intensity with an increase in Eu content, possibly due to concentration quenching. The same effect at relatively low Eu^{2+} concentrations has been reported for $Sr_5(PO_4)_3Cl:Eu^{2+}$ in a previous work.[40] The calculated FWHM values were 37 nm regardless of Eu content. While the PL spectra are dominated by Eu^{2+} emission, the emission of Eu^{3+} is also seen in the range from *ca.* 575 to 710 nm due to the overlap of the excitation spectra of Eu^{2+} and Eu^{3+} ions. The emission lines centered at around 591, 616, and 698 nm correspond to the $^5D_0 \rightarrow {}^7F_1$, $^5D_0 \rightarrow {}^7F_2$, and $^5D_0 \rightarrow {}^7F_4$ intraconfigurational $[Xe]4f^6 \rightarrow [Xe]4f^6$ transitions of Eu^{3+} ions, respectively.[41] As seen, the Eu^{2+}/Eu^{3+} emission intensity ratio decreased with an increase in Eu concentration. A possible reason is concentration quenching of the Eu^{2+} emission, whereas concentration quenching of Eu^{3+} was not achieved. Analogical observation for $Sr_5(PO_4)_3Cl:Eu^{2+/3+}$ system was previously reported by Chen *et al.*[28] Moreover, a similar effect was observed for other Eu^{2+}/Eu^{3+}-containing inorganic matrices, including crystalline materials and glasses.[42,43] The calculated QY values varied in the range from 6% to 42% being the highest for the sample with 0.1% of Eu and the lowest for 2% of Eu (Table S1).

The shape of the emission band of Eu^{2+} is asymmetrical, suggesting the presence of Eu^{2+} ions in multiple crystallographic sites. The deconvolution of the PL spectrum with 2 Gaussian components resulted in good agreement between the cumulative fit and the experimental data (Fig. 3c). The presence of 2 sub-spectra centered at 21 357 cm^{-1} (468 nm) and 22 456 cm^{-1} (445 nm) correlates well with the crystal structure of $Sr_5(PO_4)_3Cl$, having 2 inequivalent Sr sites.[22]

The emission of materials doped with mixed-valence Eu ions can be tuned by selecting a specific excitation wavelength. In some cases, this approach allows for the excitation of only one or both Eu species, resulting in the tunable emission.[44,45] Moreover, this approach enables tuning of emission in materials where Eu^{2+} ions occupy multiple crystallographic sites.[45] Fig. 3d shows normalized PL spectra obtained under systematically varying excitation wavelength with a step of 10 nm. In our case, under a particular excitation wavelength, it was possible to eliminate the emission from Eu^{3+} species (*e.g.*, 330–350 nm), whereas in general, the spectral changes were insignificant, as reflected in negligible Eu^{2+} emission band broadening and minor fluctuations in the Eu^{2+}/Eu^{3+} emission ratio. As expected, such variations did not result in a perceptible shift of the CIE coordinates (Fig. S7).

The quantification of Eu^{2+} and Eu^{3+} in mixed-valence materials is challenging, especially in the case of low doping levels. A direct comparison of the emission intensities of Eu^{2+} and Eu^{3+} ions is unsuitable due to the different types of transitions that occur in these ions. Previously, for this purpose, Dereń *et al.* employed magnetic susceptibility measurements;[46] however, we do not have the technical possibilities for such measurements. We also measured the PL spectra under the excitation wavelengths characteristic of Eu^{3+} to see if the Eu^{3+} emission could prevail. Fig. 3e demonstrates the PL spectra of the $Sr_5(PO_4)_3Cl$:0.25%Eu sample under excitation at 361, 374, 380, and 393 nm. Evidently, a broadband emission of Eu^{2+} dominated the spectra in all cases, and the emission of Eu^{3+} in the 580–710 nm range constituted only 0.74%–2.9% of the entire emission, depending on the λ_{ex}. This observation suggests that the majority of Eu ions exist in the reduced divalent state.

Fig. 3f shows the PL decay curves of $Sr_5(PO_4)_3Cl:Eu$ powders when the samples were excited at 405 nm, and the emission was monitored at 445 nm. The single-exponential decay model can be applied to the PL decay curves of all samples. The calculated PL lifetime values (τ) were independent of Eu content and varied only insignificantly from 527 to 534 ns, which is comparable with previously published data.[40] Overall, it can be concluded that the room temperature photoluminescent properties of our synthesized materials agree well with those of $Sr_5(PO_4)_3Cl:Eu^{2+}$ prepared in a reducing atmosphere in terms of emission spectral shape, position, and PL lifetime values.[22,40]

The self-reduction of Eu in alkaline-earth metal phosphates is usually explained by the charge compensation model.[7,28,47] According to this model, during the non-equivalent substitution in the crystal lattice, two Eu^{3+} ions replace three M^{2+} ions, which results in the simultaneous formation of two types of defects: (I) two Eu_M defects with a single positive charge and (II) one M^{2+} vacancy with a double negative charge to keep the neutrality of the material. These negatively charged vacancies act as electron donors, while positively charged Eu^{3+} defects act as electron acceptors. The interaction of the defects leads to the reduction of Eu^{3+} ions to the divalent state, which is further protected from the oxidizing air atmosphere by the phosphate framework. Such a mechanism can be reasonably suggested for the $Sr_5(PO_4)_3Cl:Eu$ system investigated in the present work and can be described by the following equations:

$$3Sr^{2+} + 2Eu^{3+} \rightarrow V''_{Sr} + 2Eu^{\bullet}_{Sr} \quad (1)$$

$$V''_{Sr} \rightarrow V^{\times}_{Sr} + 2e^- \quad (2)$$

$$2Eu^{\bullet}_{Sr} + 2e^- \rightarrow 2Eu^{\times}_{Sr} \quad (3)$$

It is worth noting that some parallel processes related to the formation of oxygen defects can influence the degree of self-reduction.[28,48,49] In the case of $Sr_5(PO_4)_3Cl$, the formation of chlorine-related defects also cannot be excluded; however it needs further investigation.

The temperature-dependent luminescent properties of $Sr_5(PO_4)_3Cl$:0.25%Eu in the 77–500 K range were further investigated (Fig. 4). The PLE spectra recorded at 77 K and 500 K at emission wavelength of 455 nm have the same shape with the maxima more expressed at low temperature (Fig. 4a). With an increase in the temperature the PL spectra demonstrated three trends associated with the intensity, emission maximum and FWHM values of the Eu^{2+}-related emission (Fig. 4b). The intensity decreased with increasing temperature due to the thermal

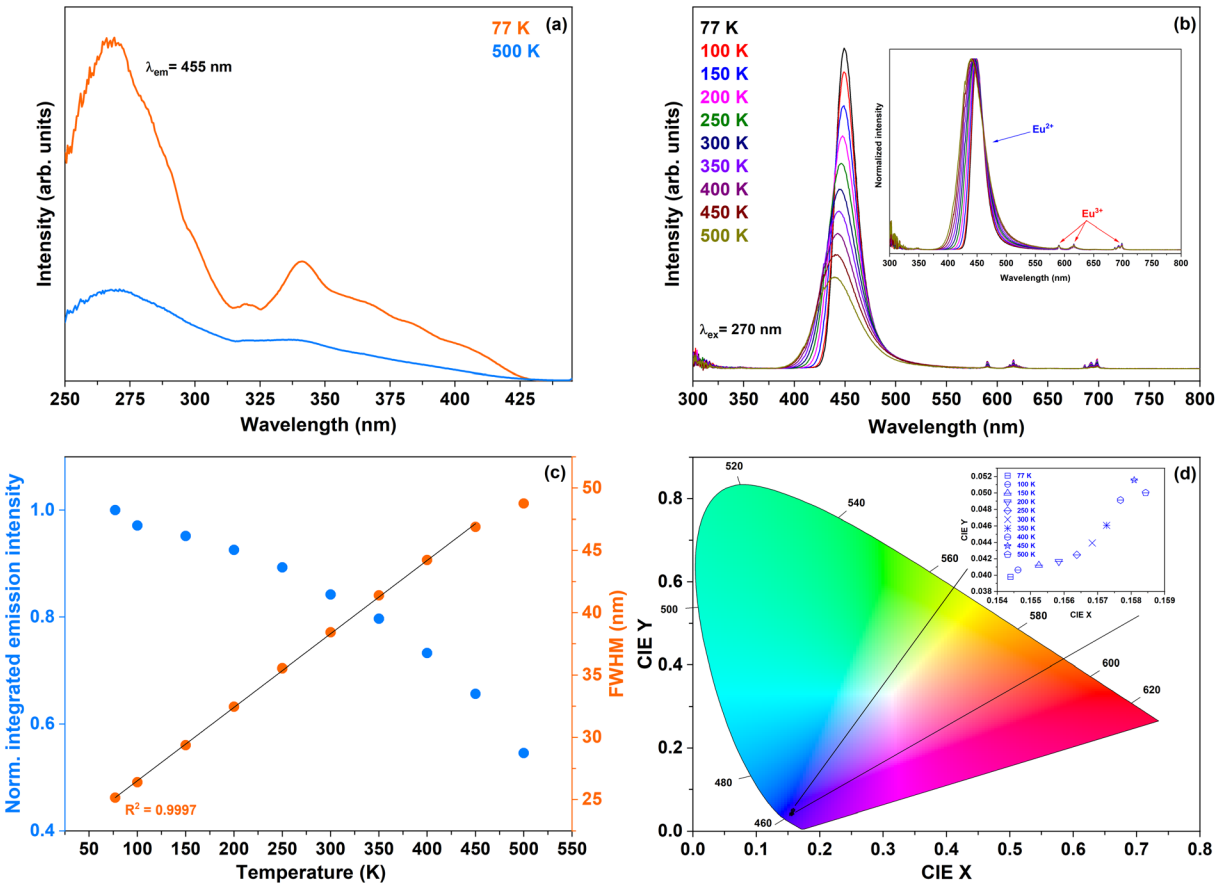

Fig. 4 Temperature-dependent PLE spectra (a); PL spectra (inset – normalized PL spectra) (b); FWHM and normalized integrated intensity values (c); and CIE 1931 chromaticity coordinates (d) of $Sr_5(PO_4)_3Cl$:0.25%Eu sample (λ_{ex} = 270 nm).

quenching. At 400 K, the integrated emission intensity constituted 73% and 87% of those at 77 and 300 K, respectively. In parallel, the linear increase in the FWHM values from 24 nm at 77 K to 47 nm at 450 K was observed (Fig. 4c). The emission maximum was stable at 449 nm in the temperature range from 77 to 150 K, followed by the gradual blue shift at higher temperatures down to 440 nm at 500 K. These results go hand in hand with the CIE 1931 chromaticity diagram (Fig. 4d), where color coordinates shift towards the center of the diagram with the temperature increase as a result of emission spectra broadening.

It is evident that exposing $Sr_5(PO_4)_3Cl$:Eu samples to ionizing radiation, such as X-rays or UV light, generates delocalized charge carriers that can become trapped in localized defect-induced energy levels within the band gap, known as charge traps. Charge traps temporarily capture and hold charge carriers, preventing them from recombining or conducting freely. The trap properties of materials are typically characterized by TSL measurements and analysis. Fig. 5a presents the TSL glow curves of the $Sr_5(PO_4)_3Cl$:0.1%Eu sample after irradiation with X-rays and UV light. Regardless of the irradiation source, two distinct glow peaks are observed with T_{max} values near 110 °C and 190 °C, indicating the presence of at least two types of charge traps. These two peaks were consistently detected across all studied samples (Fig. S8). In most cases, the number of discrete TSL peaks corresponds to the number of trap types in the material.[50] The TSL emission spectra corresponding to both glow peaks exhibit the characteristic broadband blue luminescence of Eu^{2+}, with no detectable emission from Eu^{3+}. However, when the X-ray exposed sample is heated to 255 °C, Eu^{3+} luminescence bands around 600 and 700 nm appear (Fig. 5b). In contrast, the UV-irradiated sample shows no signs of Eu^{3+} emission, although it is worth noting that the overall luminescence intensity in this high-temperature range is significantly weaker than at the TSL peak temperatures. The differences could be explained by both the formation of X-ray-induced charge traps near Eu^{3+} or the partial ionization of Eu^{2+} to Eu^{3+} during the excitation.

For further investigation of trap properties, an X-ray irradiated $Sr_5(PO_4)_3Cl$:0.1%Eu sample was selected. The widely recognized T_{max}–T_{stop} and initial rise analysis (IRA) techniques were applied, and the results are illustrated in Fig. 6. These methods are analytical approaches in TSL used to determine the number of trap types and the activation energy (E_a) of charge traps in materials by examining how glow peaks shift under controlled preheating-cooling-TSL cycles. The methods are detailed elsewhere.[51–53] As expected, the T_{max}–T_{stop} plot (blue dots, Fig. 6c) indicates the presence of two types of traps.

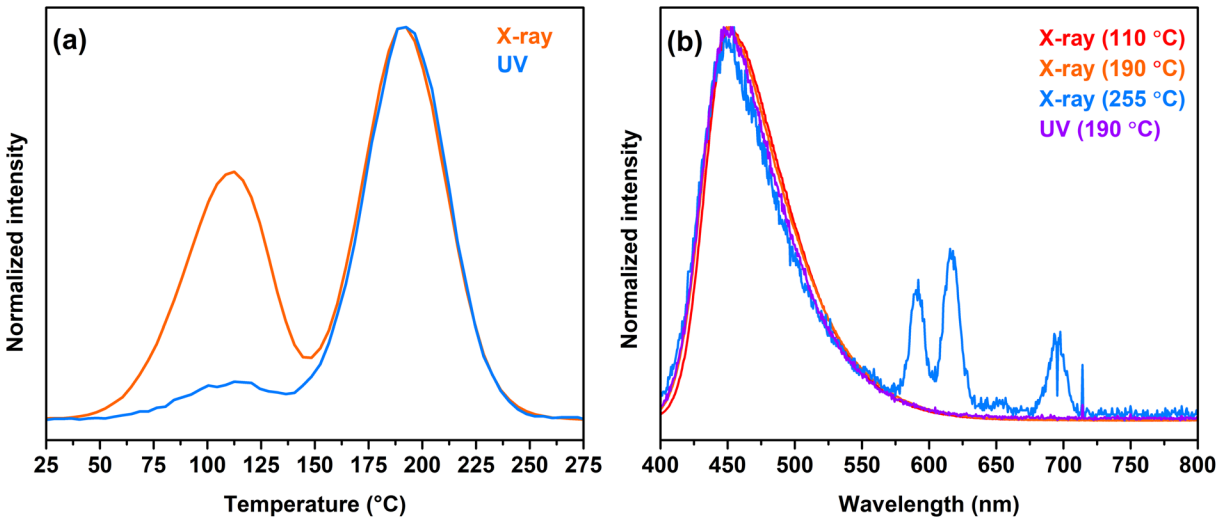

Fig. 5 TSL glow curves of the $Sr_5(PO_4)_3Cl$:0.1%Eu sample after irradiation with X-rays or UV for 60 s (a); normalized TSL spectra of the $Sr_5(PO_4)_3Cl$:0.1%Eu sample at different temperatures after irradiation with X-rays or UV (b).

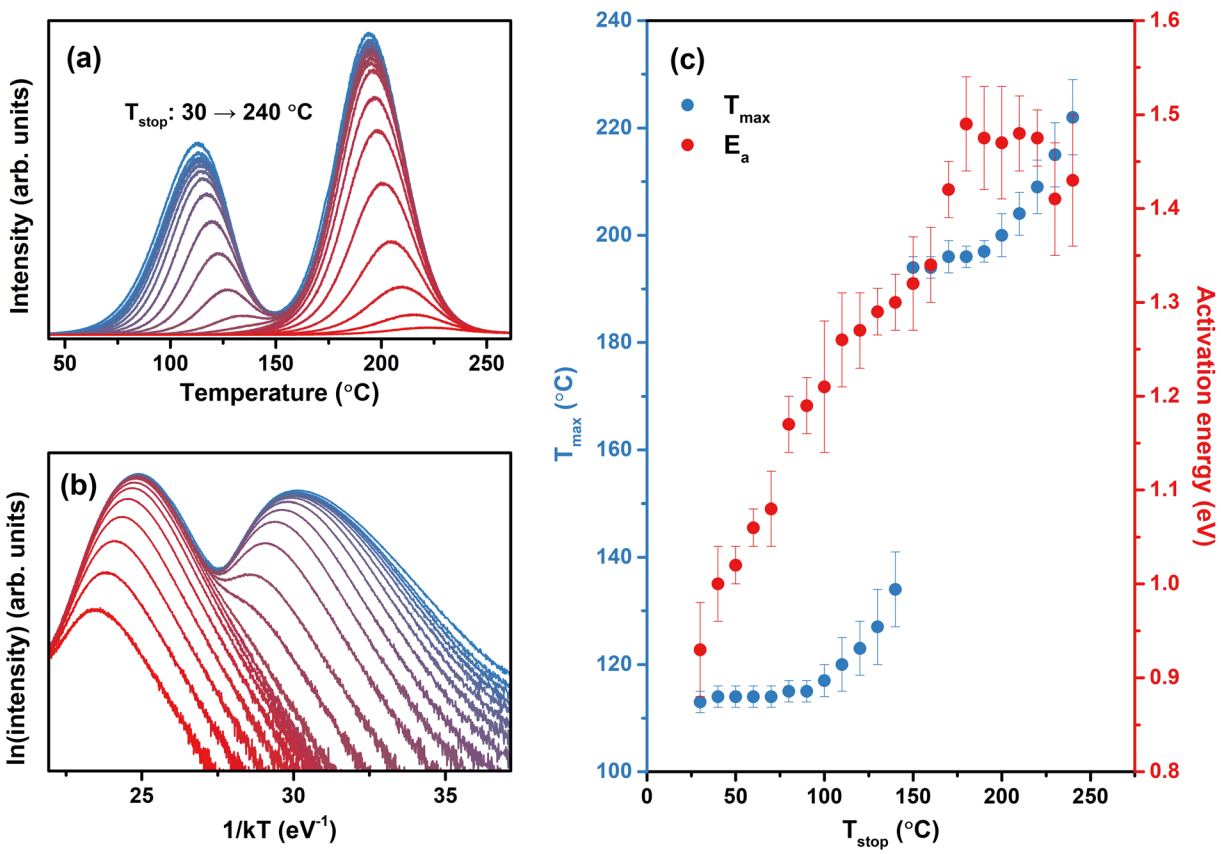

Fig. 6 TSL glow curves of the $Sr_5(PO_4)_3Cl$:0.1%Eu sample after preheating to various T_{stop} values ranging from 30 to 240 °C in 10 °C increments, when the sample was irradiated with X-rays for 20 s before each preheating (a); IRA plots of the glow curves obtained from the T_{max}–T_{stop} experiment (b), and T_{max}–T_{stop} and E_a–T_{stop} plots (c).

However, the determined E_a values (red squares, Fig. 6c) are less conclusive. The deep trap with T_{max} = 190 °C is characterized as a discrete trap with an activation energy value of approximately 1.45 ± 0.10 eV. Meanwhile, the shallow trap with T_{max} = 110 °C cannot be defined by a single E_a value and gradually varies from 0.93 to 1.34 eV with increased preheating temperature (T_{stop}). This suggests that the T_{max} = 110 °C glow peak does not correspond to a discrete trapping site and is

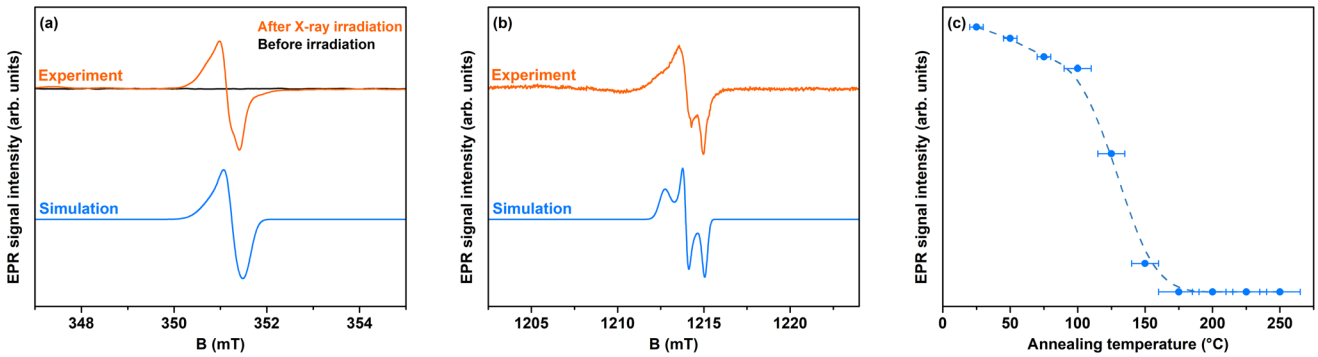

Fig. 7 Simulations of X-band (a) and Q-band (b) EPR spectra of the $Sr_5(PO_4)_3Cl$:0.1%Eu sample after irradiation with X-rays; annealing kinetics of the X-ray induced radicals (c).

more likely associated with a quasi-continuous trap distribution. The appearance of trap distributions is anticipated in the case of the same type of trap in a highly disordered site.[54,55] Although all obtained E_a values are somewhat deep, a persistent luminescence signal of Eu^{2+} can be detected for several hours after X-ray irradiation (Fig. S9).

EPR spectra measurements were performed to gain additional insights into the charge trapping processes in $Sr_5(PO_4)_3Cl$:Eu. As shown in Fig. 7a, paramagnetic radiation-induced radicals form upon X-ray irradiation. The EPR spectrum recorded at Q-band microwave frequency (Fig. 7b) highlights the anisotropy in signal shape, indicating anisotropy of the g-factor. The experimental spectra recorded at both microwave frequencies can be simulated using electronic spin $S = 1/2$ with $g_1 = 2.0038 \pm 0.0005$, $g_2 = 2.0018 \pm 0.0005$, and $g_3 = 1.9999 \pm 0.0005$. Various types of radicals in phosphate materials have been identified based on unpaired spin S interaction with magnetic ^1H, ^{14}N, or ^{31}P nuclei.[56–59] However, as no EPR spectrum hyperfine structure could be resolved in our case, such assignments are unlikely. The determined g-factor values are similar to those reported for CO_2^--type radicals in different hosts.[59] It could be possible that a trace amount of carbon-containing impurities, such as carbonates, could lead to the formation of similar defects in $Sr_5(PO_4)_3Cl$. Furthermore, thermal annealing in the 100–150 °C range (Fig. 7c) is correlated with the first peak observed in TSL glow curves (Fig. 5), which signifies the role of detected radicals in optical processes of the material.

In summary, the molten salt synthesis offers a relatively simple route for the preparation of Eu^{2+}-doped $Sr_5(PO_4)_3Cl$, demonstrating an efficient Eu self-reduction. Although a limitation in terms of Eu doping level was observed, potentially it could be overcome by changing the flux composition by adding alkali metal chlorides, thereby reducing the percentage of $SrCl_2$. The use of mixed flux in its turn could also lead to the synthesis of $Sr_5(PO_4)_3Cl$:Eu^{2+} at significantly lower temperatures. Photoluminescent characteristics of the obtained materials were comparable to those of $Sr_5(PO_4)_3Cl$:Eu^{2+} synthesized in a reducing atmosphere. The efficient Eu^{2+} emission, combined with slightly tunable photoluminescence and persistent luminescence, shows the potential of $Sr_5(PO_4)_3Cl$ for practical applications.

4. Conclusions

$Sr_5(PO_4)_3Cl$:Eu^{2+} powders were successfully synthesized in an air atmosphere from $Sr_3(PO_4)_2$:Eu^{3+} precursors. The phase transformation from $Sr_3(PO_4)_2$:Eu to $Sr_5(PO_4)_3Cl$:Eu was achieved in molten $SrCl_2$ and accompanied by the self-reduction of Eu^{3+} to Eu^{2+}. Although the PL spectra of the synthesis products were clearly dominated by the broadband emission characteristic of Eu^{2+}, significantly weaker emission in the red region was also detected and ascribed to Eu^{3+}, suggesting an incomplete Eu reduction. It was found that the Eu^{2+}/Eu^{3+} emission intensity ratio decreased with an increase in Eu concentration. Overall, the photoluminescent properties of the synthesized materials agreed well with those reported in literature for $Sr_5(PO_4)_3Cl$:Eu^{2+} prepared in a reducing atmosphere in terms of emission spectral shape, emission maximum, and the PL lifetime. The investigation of trap properties indicated the presence of two types of traps in the materials. Although all obtained E_a values were deep, a weak persistent luminescence signal of Eu^{2+} can be detected for several hours after X-ray irradiation. The results of EPR spectroscopy confirmed the formation of paramagnetic radiation-induced radicals and agreed well with the results of TSL.

Conflicts of interest

There are no conflicts to declare.

Data availability

The data supporting this study have been included within the article and the supplementary information (SI). Supplementary information is available. See DOI: https://doi.org/10.1039/d5dt02634b.

Acknowledgements

This project has received funding from the Research Council of Lithuania (LMTLT), agreement no. S-MIP-25-26. V. P. acknowledges LZP grant 2023/1-0063.

References

1 S. Zhao, Y. Han, S. Lian and J. Zhang, *Dalton Trans.*, 2025, **54**, 8745–8763.
2 P. Dorenbos, *J. Lumin.*, 2003, **104**, 239–260.
3 Z. Yang, Y. Zhao, Y. Zhou, J. Qiao, Y.-C. Chuang, M. S. Molokeev and Z. Xia, *Adv. Funct. Mater.*, 2022, **32**, 2103927.
4 C. Dou, Z. Song and Q. Liu, *J. Mater. Chem. C*, 2024, **12**, 11209–11241.
5 J. Zou, L. Li, X. Fang, L. Chen and H. Guo, *J. Mater. Chem. C*, 2025, **13**, 14808–14813.
6 X. Lin, H. Han, M. Yang, Z. Yuan, Z. Chen, W.-G. Li, H. Kang, S. Zhang, Y. Zhang, Y.-X. Chen, T. Tian and H. Pang, *Adv. Mater.*, 2025, **37**, 2417420.
7 S. Khan, H.-W. Zheng, H. Jiao, S. Saleem, Z. Gul, J. Y. Al-Humaidi, A. A. Bahir, R. H. Althomali, A. Ali and M. M. Rahman, *Rev. Inorg. Chem.*, 2024, **44**, 547–567.
8 M. Peng, Z. Pei, G. Hong and Q. Su, *J. Mater. Chem.*, 2003, **13**, 1202–1205.
9 R.-K. Du, X.-L. He, T.-Z. Xiao, Y.-F. Xiang, L. Zhong, L. Zhou, J.-C. Zhang, D.-Q. Yao, T.-Y. Sun and M.-M. Wu, *Laser Photonics Rev.*, 2025, **19**, 2401211.
10 H. Yu, F. Ruan, L. Chen and D. Deng, *Opt. Mater.*, 2020, **100**, 109678.
11 W. Teng, H. Dong, C. Hu, X. Yang, J. Wang, X. Liang, B. Yang, J. Ru, B. Teng and D. Zhong, *J. Lumin.*, 2024, **269**, 120524.
12 R. Lu, X. Zhang, Y. Fang, X. Wu, M. Jia, K. Wang, J. Wu, Q. Li and Z. Sun, *Laser Photonics Rev.*, 2024, **18**, 2400409.
13 R. D. Shannon, *Acta Crystallogr., Sect. A*, 1976, **32**, 751–767.
14 M. Gu, W. Li, L. Jiang and X. Li, *Acta Biomater.*, 2022, **148**, 22–43.
15 M. Back, J. Cangiotti, J. Stadulis, A. Katelnikovas, M. G. Brik, P. Riello and A. Zarkov, *Adv. Opt. Mater.*, 2025, e03109, DOI: 10.1002/adom.202503109.
16 H.-S. Roh, S. Lee, F. Qin, S. Caliskan, C. Yoon and J.-K. Lee, *ACS Appl. Nano Mater.*, 2018, **1**, 4483–4490.
17 K. Szyszka, M. Kardach, D. Szymański and R. J. Wiglusz, *J. Lumin.*, 2024, **275**, 120788.
18 Y. Zhang, Z. Zhou and B. Mei, *J. Eur. Ceram. Soc.*, 2024, **44**, 5744–5751.
19 X. Liu, B. Mei and G. Tan, *J. Eur. Ceram. Soc.*, 2024, **44**, 4975–4984.
20 R. A. Talewar, S. Mahamuda, A. S. Rao, V. M. Gaikwad, P. D. Belsare and S. V. Moharil, *J. Lumin.*, 2020, **222**, 117118.
21 L. Fu, D. Wu, Y. Xiao, W. Zou, J. Kuang, Y. Liang, F. Du, J. Peng and X. Ye, *J. Alloys Compd.*, 2021, **878**, 160354.
22 D. Kim, S.-C. Kim, J.-S. Bae, S. Kim, S.-J. Kim and J.-C. Park, *Inorg. Chem.*, 2016, **55**, 8359–8370.
23 L. Zhou, H. Liang, P. A. Tanner, S. Zhang, D. Hou, C. Liu, Y. Tao, Y. Huang and L. Li, *J. Mater. Chem. C*, 2013, **1**, 7155–7165.
24 X. Chen, P. Dai, X. Zhang, C. Li, S. Lu, X. Wang, Y. Jia and Y. Liu, *Inorg. Chem.*, 2014, **53**, 3441–3448.
25 K. Liu, T. Wen, C. Li, Y. Ma, D. Jiang, B. Yue and Y. Wang, *J. Mater. Chem. C*, 2023, **11**, 2162–2168.
26 Z. Ma, S. Fang, Y. Bai, W. Wei and Z. Wang, *Mater. Today Chem.*, 2024, **36**, 101917.
27 Y. Deng, S. Yi, J. Huang, W. Zhao and X. Fang, *J. Rare Earths*, 2013, **31**, 962–968.
28 J. Chen, Y. Liang, Y. Zhu, S. Liu, H. Li and W. Lei, *J. Lumin.*, 2019, **214**, 116569.
29 Y. Song, H. You, M. Yang, Y. Zheng, K. Liu, G. Jia, Y. Huang, L. Zhang and H. Zhang, *Inorg. Chem.*, 2010, **49**, 1674–1678.
30 H. Zou, M. Yan, G. Wang, B. Yuan, J. Huang, F. Gao, Y. Sheng, K. Zheng and Y. Song, *Powder Technol.*, 2014, **254**, 579–582.
31 L. Klimkeviciene, E. Parafjanovic, V. Klimkevicius and A. Katelnikovas, *Ceram. Int.*, 2024, **50**, 38456–38461.
32 S. Stoll and A. Schweiger, *J. Magn. Reson.*, 2006, **178**, 42–55.
33 M. Kemere, U. Rogulis and J. Sperga, *J. Alloys Compd.*, 2018, **735**, 1253–1261.
34 K. Szyszka, N. Nowak, R. M. Kowalski, J. Zukrowski and R. J. Wiglusz, *J. Mater. Chem. C*, 2022, **10**, 9092–9105.
35 D. Karoblis, O. C. Stewart Jr., P. Glaser, S. E. El Jamal, A. Kizalaite, T. Murauskas, A. Zarkov, A. Kareiva and S. L. Stoll, *Inorg. Chem.*, 2023, **62**, 10635–10644.
36 S. L. Bennett, C. B. Finch, H. L. Yakel, J. Brynestad and G. W. Clark, *J. Cryst. Growth*, 1977, **41**, 309–310.
37 B. O. Fowler, *Inorg. Chem.*, 1974, **13**, 194–207.
38 E. Kabasinskas, D. Karoblis, D. Griesiute, E. Raudonyte-Svirbutaviciene, S. Pazylbek, R. Lemezis, V. Klimavicius, A. Kareiva and A. Zarkov, *Ceram. Int.*, 2024, **50**, 16844–16851.
39 A. C. Taş, *J. Am. Ceram. Soc.*, 2001, **84**, 295–300.
40 J. Zheng, Q. Cheng, S. Wu, Z. Guo, Y. Zhuang, Y. Lu, Y. Li and C. Chen, *J. Mater. Chem. C*, 2015, **3**, 11219–11227.
41 Z. Hao, J. Zhang, X. Zhang and X. Wang, *Opt. Mater.*, 2011, **33**, 355–358.
42 X. Jiang, Y. Guo, L. Wang and Q. Zhang, *Ceram. Int.*, 2023, **49**, 28729–28740.
43 H. Chen, C. Zhou, X. Chen, C. Min, S. Lin, Y. Li, T. Zhou, J. Kang, C. Shi, C. Shao, P. Han, W. Strek, H. Chen and L. Zhang, *J. Am. Ceram. Soc.*, 2025, **108**, e20237.
44 B. Yu, Y. Li, Y. Wang, N. Li, P. Xiao, D. Liu and L. Geng, *Inorg. Chem.*, 2022, **61**, 2463–2475.
45 S. Pazylbek, J. Stadulis, G. Doke, A. Antuzevics, V. Pankratov, G. Merkininkaite, A. Katelnikovas and A. Zarkov, *Dalton Trans.*, 2025, **54**, 8625–8634.
46 P. J. Dereń, D. Stefańska, M. Ptak and P. Wiśniewski, *J. Phys. Chem. C*, 2021, **125**, 24505–24514.
47 E. V. Sipina, D. A. Spassky, N. R. Krutyak, V. A. Morozov, E. S. Zhukovskaya, A. A. Belik, M. S. Manylov, B. I. Lazoryak and D. V. Deyneko, *Materials*, 2023, **16**, 1383.

48 H. Li and Y. Wang, *Inorg. Chem.*, 2017, **56**, 10396–10403.
49 H. Wang, K. Su, L. Mei, Q. Guo and L. Liao, *Inorg. Chem.*, 2023, **62**, 12468–12479.
50 A. J. J. Bos, *Radiat. Meas.*, 2006, **41**, S45–S56.
51 S. W. S. McKeever, *Phys. Status Solidi A*, 1980, **62**, 331–340.
52 V. Pagonis, G. Kitis and C. Furetta, *Numerical and practical exercises in thermoluminescence*, Springer New York, NY, 2006.
53 A. Antuzevics, G. Doke, G. Krieke, P. Rodionovs, D. Nilova, J. Cirulis, A. Fedotovs and U. Rogulis, *Materials*, 2023, **16**, 1776.
54 K. Van den Eeckhout, A. J. J. Bos, D. Poelman and P. F. Smet, *Phys. Rev. B: Condens. Matter Mater. Phys.*, 2013, **87**, 045126.
55 G. Krieke, G. Doke, A. Antuzevics, R. Ignatans, I. Pudza and A. Kuzmin, *J. Alloys Compd.*, 2023, **957**, 170421.
56 D. V. Shurtakova, B. V. Yavkin, G. V. Mamin, S. B. Orlinskii, V. P. Sirotinkin, A. Y. Fedotov, A. Shinkarev, A. Antuzevics, I. V. Smirnov, V. I. Tovtin, E. E. Starostin, M. R. Gafurov and V. S. Komlev, *Radiat. Res.*, 2020, **195**, 200–210, 211.
57 A. Antuzevics, J. Cirulis, G. Krieke, D. Griesiute, A. Beganskiene, A. Kareiva, A. Dubauskas, V. Klimavicius and A. Zarkov, *Mater. Chem. Phys.*, 2023, **310**, 128479.
58 A. Antuzevics, G. Doke, G. Krieke, J. Stadulis, A. Beganskiene, A. Kareiva, C.-Y. Su, H.-W. Fang and A. Zarkov, *J. Alloys Compd.*, 2025, **1012**, 178525.
59 P. Fattibene and F. Callens, *Appl. Radiat. Isot.*, 2010, **68**, 2033–2116.